Experimental investigation of the characteristics of radioactive beams for heavy ion therapy

Andrew Chacon, Benjamin James, Linh Tran, Susanna Guatelli
Centre for Medical Radiation Physics, University of Wollongong, Wollongong, NSW 2522, Australia

Lachlan Chartier, Dale Prokopvich
Australian Nuclear Science and Technology Organisation, Lucas Heights, NSW 2234, Australia

Daniel R. Franklin
University of Technology Sydney, Ultimo, NSW 2007, Australia

Akram Mohammadi, Fumihiko Nishikido, Yuma Iwao, Go Akamatsu, Sodai Takyu, Hideaki Tashima, Taiga Yamaya
National Institute of Radiological Sciences (NIRS), National Institutes for Quantum and Radiological Science and Technology, 4-9-1 Anagawa, Inage-ku, Chiba 263-8555, Japan

Katia Parodi
Department of Medical Physics, Ludwig-Maximilians-Universit at M unchen, Garching b. M unchen, Germany

Anatoly Rosenfeld
Centre for Medical Radiation Physics, University of Wollongong, Wollongong, NSW 2522, Australia

Mitra Safavi-Naeini
Australian Nuclear Science and Technology Organisation, Lucas Heights, NSW 2234, Australia

Version typeset April 5, 2020

Mitra Safavi-Naeini. email: mitras@ansto.gov.au

Abstract

Purpose: This work has two related objectives. The first is to estimate the relative biological effectiveness of two radioactive heavy ion beams based on experimental measurements, and compare these to the relative biological effectiveness of corresponding stable isotopes to determine whether or not they are therapeutically equivalent. The second aim is to quantitatively compare the quality of images acquired post-irradiation using an in-beam whole-body positron emission tomography scanner for range verification quality assurance.

Methods: The energy deposited by monoenergetic beams of ^{11}C at 350 MeV/u, ^{15}O at 250 MeV/u, ^{12}C at 350 MeV/u and ^{16}O at 430 MeV/u were measured using a cruciform transmission ionisation chamber in a water phantom at the Heavy Ion Medical Accelerator in Chiba (HIMAC), Japan. Dose-mean lineal energy was measured at various depths along the path of each beam in a water phantom using a silicon-on-insulator mushroom microdosimeter. Using the modified microdosimetric kinetic model, the relative biological effectiveness at 10% survival fraction of the radioactive ion beams was evaluated and compared to that of the corresponding stable ions along the path of the beam. Finally, the post-irradiation distributions of positron annihilations resulting from the decay of positron-emitting nuclei were measured for each beam in a gelatin phantom using the in-beam whole-body positron emission tomography scanner at HIMAC. The depth of maximum positron-annihilation density was compared with the depth of maximum dose deposition and the signal-to-background ratios were calculated and compared for images acquired over 5 minutes and 20 minutes post irradiation of the phantom.

Results: In the entrance region, the RBE_{10} was 1.2 ± 0.1 for both ^{11}C and ^{12}C beams, while for ^{15}O and ^{16}O it was 1.4 ± 0.1 and 1.3 ± 0.1, respectively. At the Bragg peak, the RBE_{10} was 2.7 ± 0.4 for ^{11}C and 2.9 ± 0.4 for ^{12}C, while for ^{15}O and ^{16}O it was 2.7 ± 0.4 and 2.8 ± 0.4, respectively. In the tail region, RBE_{10} could only be evaluated for carbon; the RBE_{10} was 1.6 ± 0.2 and 1.5 ± 0.1 for ^{11}C and ^{12}C, respectively.

Positron emission tomography images obtained from gelatin targets irradiated by radioactive ion beams exhibit markedly improved signal-to-background ratios compared to those obtained from targets irradiated by non-radioactive ion beams, with 5-fold and 11-fold increases in the ratios calculated for the ^{15}O and ^{11}C images compared with the values obtained for ^{16}O and ^{12}C, respectively. The difference between the depth of maximum dose and the depth of maximum positron annihilation density is 2.4±0.8 mm for ^{11}C, compared to -5.6 ± 0.8 mm for ^{12}C and 0.9 ± 0.8 mm for ^{15}O versus -6.6 ± 0.8 mm for ^{16}O.

Conclusions: The RBE_{10} values for ^{11}C and ^{15}O were found to be within the 95% confidence interval of the RBEs estimated for their corresponding stable isotopes across each of the regions in which it was evaluated. Furthermore, for a given dose, ^{11}C and ^{15}O beams produce much better quality images for range verification compared with ^{12}C and ^{16}O, in particular with regards to estimating the location of the Bragg peak.

I. Introduction

Heavy ion therapy (HIT) is a form of radiotherapy in which highly accelerated ions are used to deliver a therapeutic dose to a treatment region[1,2,3]. The major advantage of HIT over conventional photon therapy is that the kinetic energy carried by the ions is deposited in a highly localised, energy-dependent region at the end of their range, known as the Bragg Peak[1,4,5]. Additionally, heavy ions have high relative biological effectiveness (RBE) in the target region, making HIT well-suited for the treatment of deep seated and radio-resistant tumours[2,3,6,7].

The dose delivered by HIT can be localised to a target with a sharply-defined distal and lateral boundary, which can result in steep dose gradients between the target volume and the surrounding tissue[5,8]. As such, there is considerable interest in accurate quality assurance (QA) techniques for heavy ion therapy which can verify that the delivered dose distribution matches the treatment plan[9,10,11,12,13,14]. One of the most promising methods for dose verification QA is to image the short-lived positron-emitting radionuclides created through nuclear fragmentation between the ions in the beam and nuclei in the target material[5,15,16,17]. There has been significant research into design and development of in-beam positron emission tomography (PET) scanners which can be positioned around the patient during treatment to measure the distribution of positron annihilations which occur during the inter-spill period of pulsed synchrotron-based irradiation (or similar) and post irradiation[9,11,12,18,19].

In-beam PET imaging can be challenging due to the low yield of positron-emitting radionuclides relative to the delivered dose, which limits the signal-to-noise ratio (SNR) of the acquired PET image, and hence the accuracy with which the treated volume can be visualised. To increase the number of annihilation photons around the particle stopping point, a positron-emitting primary beam can be used[20,21,22,23,24,25,26,27]. Since the PET signal is now generated from unfragmented positron-emitting primary ions in addition to positron-emitting fragmentation products, the SNR of the resulting images is greatly improved[28,29]. This will also result in a stronger correlation between the activity peak and the dose peak compared to non-radioactive beams, since most of the radioactive ions decay near their stopping point in the vicinity of the Bragg peak. In previous work, we have extensively characterised the use of radioactive ions and compared them to their corresponding stable isotopes using the Geant4 Monte Carlo simulation framework, including spatio-temporal

analysis of positron-emitting fragmentation product distribution and simulated acquisition of PET images[27].

The relative biological effectiveness of a radiation field can be evaluated using the modified microdosimetric kinetic model (MKM) together with an experimentally-measured microdosimetric spectrum, as proposed by Kase et al.[6,30]. Previous studies by Tran et al. have used a silicon-on-insulator mushroom microdosimeter, developed by the University of Wollongong's Centre for Medical Radiation Physics (CMRP), to measure the microdosimetric properties of ^{12}C, ^{14}N, and ^{16}O ion beams and hence estimate the relative biological effectiveness of these beams[31,32,33]. However, to date, the RBE of therapeutic radioactive heavy ion beams has not been experimentally evaluated. Therefore, to enable correct treatment planning with radioactive heavy ion beams, it is essential to measure their microdosimetric properties and hence evaluate their RBEs, and compare them to those of the corresponding stable ion species.

In this work, the relative biological effectiveness (RBE_{10}) of therapeutic monoenergetic ^{11}C and ^{15}O heavy ion beams with energies of at 350 MeV/u and 250 MeV/u, respectively, were experimentally estimated for 10% survival probability of human salivary gland cells, using the microdosimetric kinetic model and compared to the corresponding respective stable ion species (^{12}C at 350 MeV/u and ^{16}O at 430 MeV/u) at multiple locations along the path of the beam. Measurements were performed in a water phantom at the Heavy Ion Medical Accelerator (HIMAC), Chiba, Japan, using the same CMRP silicon-on-insulator mushroom microdosimeter previously used by Tran et al. for measuring the microdosimetric properties of the non-radioactive ion species. Finally, post-irradiation PET images of a gelatin phantom were acquired for all radioactive and stable ion beams using the NIRS in-beam whole-body depth of interaction positron emission tomography (DOI-PET) scanner[34]. Positron annihilation yield profiles were estimated along the path of the beam, and the location of maximum annihilation density compared with the position of the peak of the depth-dose curves. The signal to background ratios (SBRs) of the PET images obtained with radioactive and stable ion beams were also compared.

The experimental configuration used for the three experiments is described in Section II.. The energy deposition measurements are detailed in Section II.A., the microdosimetry measurements are discussed in Section II.C., and finally, details about the PET measurements

are presented in Section II.D.. Experimental results are presented and discussed in Section III.: energy deposition measurements in Section III.A., microdosimetric measurements in Section III.C. and PET measurements in Section III.D.. A final summary and conclusion of the work is presented in Section IV..

II. Materials and Methods

All experimental measurements were performed at the special physics beamline at the Heavy Ion Medical Accelerator in Chiba, Japan. The beam parameters used for the experiments are listed in Table 1. Beam spill periods were 3.3 s, consisting of a beam-on time of 1.9 s followed by a beam-off time of 1.4 s. The production of ^{15}O at HIMAC's secondary beam course is presently optimised for an energy of 250 MeV/u and is produced from a 430 MeV/u ^{16}O beam passing through a 60 mm beryllium target (resulting in an ^{15}O beam with 97% purity); by contrast, ^{11}C is produced from a ^{12}C beam passing through a 51 mm beryllium target, with several primary beam energies available such that ^{11}C and ^{12}C can both be produced at 350 MeV/u. The details of these production methods have been described elsewhere[10,21,26,29].

II.A. Energy deposition

To obtain depth-dose and transverse profiles for each ion beam, the energy deposited by 350 MeV/u ^{11}C, 350 MeV/u ^{12}C, 250 MeV/u ^{15}O and 430 MeV/u ^{16}O ion beams was measured as a function of depth and lateral/vertical displacement in a water phantom. A cruciform transmission ionisation chamber array, positioned normal to the beam and mounted on a linear actuator with a stepping resolution of 0.1 mm was moved parallel to

Table 1: Nominal beam parameters

Ion	Energy (MeV/u)	Momentum acceptance (%)	Beam intensity (pps)
^{11}C	350	±2.5	1.03×10^{7}
^{12}C	350	±0.1	2.63×10^{6}
^{15}O	250	±2.5	6.42×10^{6}
^{16}O	430	±0.1	6.42×10^{6}

the path of the beam (Figure 1 (a) and (b)). The data were normalised to a beam monitor in the beam line to compensate for possible beam intensity fluctuations.

II.B. Beam geometry

The two-dimensional transverse beam size was calculated by fitting a 2D Gaussian function to the transverse dose profiles at the shallowest depth. The energy deposited for each beam was normalised to that measured at the first physically measurable depth in the phantom (26.1 mm).

II.C. Microdosimetry and RBE

The CMRP silicon-on-insulator mushroom microdosimeter was used to measure the microdosimetric properties of each ion beam. The microdosimeter was placed in a waterproof PMMA sheath, submerged in a water phantom, and aligned with the centre of the beam path at both ends of its range of travel using precise laser measurement instruments. The microdosimeter was connected to an overhead stepper motor driver with a stepping resolution of 0.1 mm and a linear travel of 200 mm along the beam axis, such that measurements can be performed at multiple points along the path of the beam (Figure 1 (c) and (d)). Due to the limited size of the water phantom, an 80 mm thick poly(methyl methacrylate), (PMMA) range shifter was used with the ^{12}C beam to shift the location of the Bragg peak to the approximate centre of the phantom. Similarly, 60 mm and 90 mm PMMA range shifters were used for the ^{11}C and ^{16}O beams, respectively; the range of the ^{15}O beam was sufficiently shallow that a range shifter was not required.

To calculate the microdosimetric properties and the RBE_{10}, the energy deposited by each particle as it traverses the sensitive volume was recorded using the CMRP silicon-on-insulator mushroom microdosimeter and an Amptek 8000A multi-channel analyser. The deposited energy was then converted to the lineal energy by dividing each energy channel by the $\langle \mathrm{l}_{\mathtt{path}} \rangle$ (mean path length) of the microdosimeter (9.1 μm) multiplied by a silicon-to-tissue correction factor of 0.58[35]. The silicon-to-tissue correction factor and $\langle \mathrm{l}_{\mathtt{path}} \rangle$ were used here rather than the mean chord length due to the directionality of a charged particle beam, as proposed by Bolst et al.[35]. The microdosimeteric dose-mean lineal energy $\overline{y_D}$ and RBE_{10}

were then calculated using the modified microdosimetric kinetic model, calculated for 10% survival probability of human salivary gland cells[6,30].

II.D. PET imaging

Two open rectangular containers with internal dimensions of 92×92×292 mm were constructed from 4 mm thick PMMA sheets and filled with gelatin solution made with distilled water, with a density of 1.001 ± 0.02 g/cm^3. Gelatin is functionally equivalent to liquid water and allows for imaging of distribution of positron-emitting fragmentation products without convection or diffusion-induced migration[1] within the medium[37]. The gelatin phantom was positioned so that the expected position of the Bragg peak was aligned with the centre of the PET scanner's field of view (Figure 1 (e) and (f)). Three repeated measurements were performed, the first and third repeat using one phantom, and the second repeat using the second phantom (with the first being reused after allowing a period of two hours to elapse for the induced radioactivity to decay to background levels). A total of 100 spills were used for ^{12}C beam, 20 spills were used for ^{11}C, while both ^{15}O and ^{16}O beams used 40 spills. The varying number of spills were needed to accommodate the variability of available particle intensity between beam types (see Table 1).

The distribution of positron annihilations resulting from the decay of positron-emitting nuclei in the irradiated target was experimentally measured for each beam using a whole-body DOI-PET scanner over periods of 5 and 20 minutes immediately post irradiation. The 5 minute acquisition allows the quality of images resulting largely from the decay of the short-lived isotopes to be evaluated and compared to an acquisition over 20 minutes which includes contributions from all three positron-emitting isotopes. A 5-minute acquisition is also of clinical interest since it does not extend the duration of the therapeutic procedure (the room cannot be entered immediately after irradiation due to the need to allow the background activity in the room to decay to safe levels). Both 5-minute and 20-minute acquisitions are feasible acquisition periods for in-beam PET systems.

PET images with a voxel size of 1.5×1.5×1.5 mm^3 were generated using the 3D ordinary Poisson ordered-subset-expectation-maximisation (3D-OP-OSEM) reconstruction algorithm.

[1]The gelatin was kept below 20°C at all times, ensuring low viscosity and hence restricting migration of positron-emitting fragments via convection or diffusion during the experiment[36].

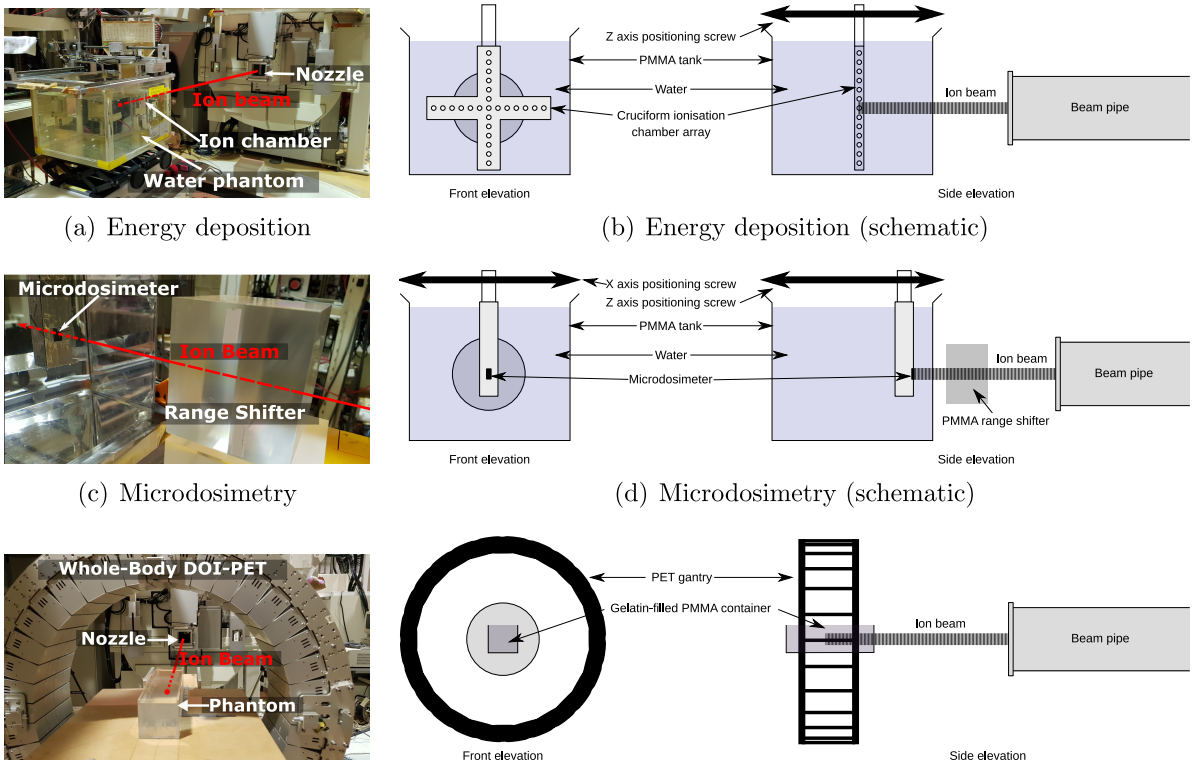

(a) Energy deposition

(b) Energy deposition (schematic)

(c) Microdosimetry

(d) Microdosimetry (schematic)

(e) PET

(f) PET (schematic)

Figure 1: The experimental configurations for all the measurements.

Normalisation, random correction and attenuation correction were applied, however, scatter correction was not necessary as scattering has a negligible impact on the estimated distribution of positron-emitting fragments in the vicinity of the Bragg peak[29]. Finally, overall image intensity was normalised by the number of primary particles.

III. Results and discussion

III.A. Energy deposition

Depth-dose curves for 350 MeV/u ^{11}C and 350 MeV/u ^{12}C ion beams in the water phantom are shown in Figure 2a, while curves for 250 MeV/u ^{15}O and 430 MeV/u ^{16}O are shown in Figure 2b. Dose is normalised to the first measured point, with a vertical dashed line drawn at the position of the Bragg peak (estimated as the depth at which maximum dose is recorded).

The depth-dose profiles of the radioactive ion beams exhibit a larger beam energy spread

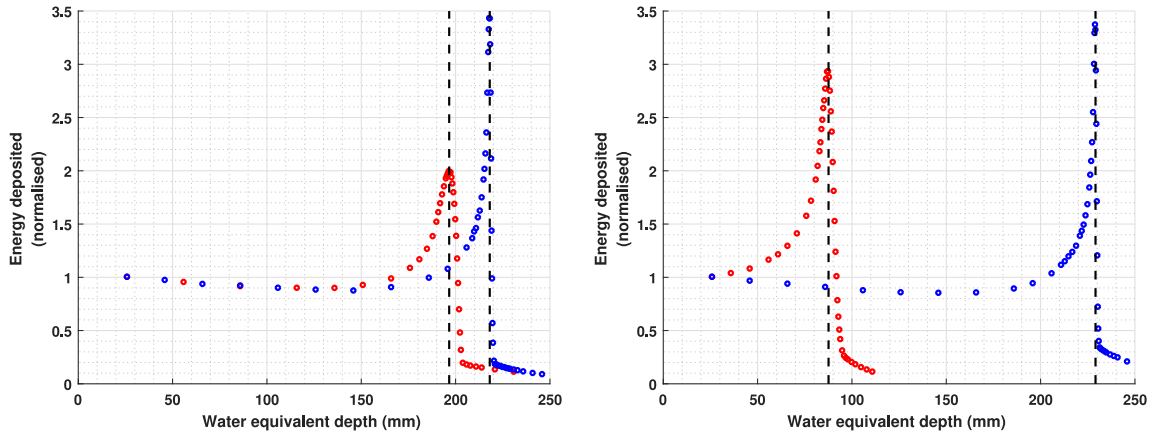

(a) Red = 350 MeV/u ^{11}C, blue = 350 MeV/u ^{12}C (b) Red = 250 MeV/u ^{15}O, blue = 430 MeV/u ^{16}O

Figure 2: Depth-dose curves for each of the evaluated ion species.

Table 2: Beam geometry

Ion	σ_x **(mm)**	σ_y **(mm)**
^{11}C	5.68	5.75
^{12}C	3.76	3.78
^{15}O	8.42	9.76
^{16}O	3.78	3.83

compared to those of the corresponding stable ion beams. This results in the normalised energy deposited at the Bragg peaks being more spread out and having a lower peak to entrance ratio than for the stable beams, even though the Bragg peak of the radioactive beams is at a shallower depth compared with the stable beam. The beam energy spread is larger for the radioactive ^{11}C and ^{15}O beams as the ions are created by fragmentation of the stable ^{12}C or ^{16}O beams, respectively (see Table 1).

III.B. Beam geometry

The Gaussian lateral size parameter σ for each beam in x and y dimensions is shown in Table 2. These were multiplied by $2\sqrt{2\ln 10}$ to compute the full width at tenth maximum (FWTM) used for delineating the region used for PET image analysis to estimate the distribution of positron annihilations described in Section III.D..

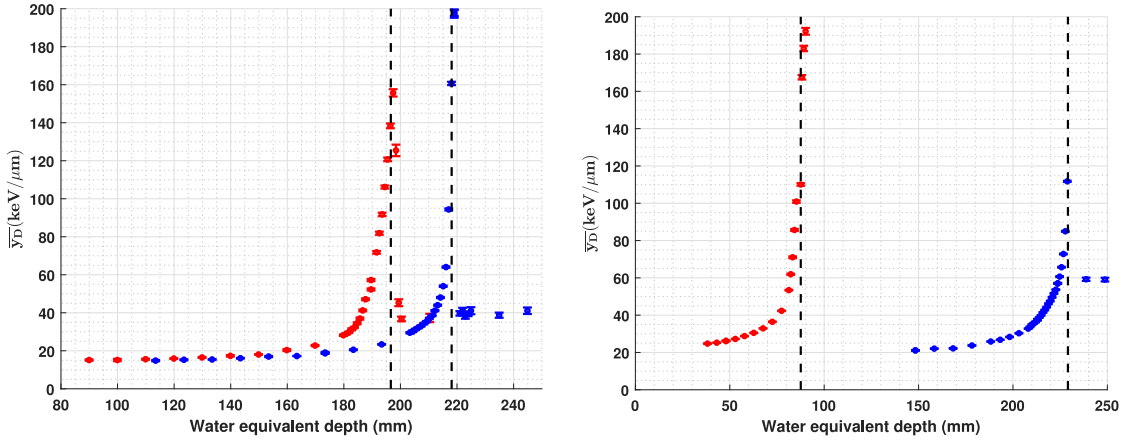

(a) Red = 350 MeV/u ^{11}C, blue = 350 MeV/u ^{12}C (b) Red = 250 MeV/u ^{15}O, blue = 430 MeV/u ^{16}O

Figure 3: The experimentally-evaluated value of $\overline{y_D}$, plotted as a function of depth, for the positron-emitting radioactive and stable isotopes of carbon and oxygen ions in a water phantom. Vertical dashed lines represent the positions of the Bragg peaks (obtained from the macroscopic depth-dose measurements).

III.C. Microdosimetry and RBE

The microdosimetric quantity $\overline{y_D}$ was measured in the water phantom, using the silicon-on-insulator mushroom microdosimeter, and is plotted as a function of depth in Figure 3a for ^{11}C/^{12}C and Figure 3b for ^{15}O/^{16}O. For each figure, a vertical dashed line is drawn at the Bragg peak (obtained from the depth-dose measurements). The values of $\overline{y_D}$ in the entrance, Bragg peak and tail regions for the carbon beams and in the entrance and Bragg peak regions for oxygen are tabulated in Table 3. $\overline{y_D}$ was not evaluated in the tail region for oxygen due to an unexpected problem during data collection for this experiment.

The evaluated RBE$_{10}$ is plotted as a function of depth for ^{11}C/^{12}C in Figure 4a and Figure 4b for ^{15}O/^{16}O. For each figure, a vertical dashed line is drawn at the Bragg peak. The evaluated RBE$_{10}$ values in the entrance, Bragg peak and tail region are tabulated in Table 4 (with the exception of the tail regions of the oxygen ion beams).

The value of $\overline{y_D}$ is in close agreement in the entrance and tail regions for ^{11}C and ^{12}C (the mean value for each isotope is within the 95% confidence interval of the other); however, in the Bragg peak region, $\overline{y_D}$ is 24% higher for ^{12}C than for ^{11}C. This may be a result of the greater momentum spread of the ^{11}C beam relative to ^{12}C. For ^{15}O, $\overline{y_D}$

Table 3: The experimentally-evaluated mean values of $\overline{y_D}$ in each region for the positron-emitting radioactive and stable isotopes of carbon and oxygen in a water phantom.

		$\overline{y_D}$ (keV/μm)		
Ion	**Energy**	**Entrance**	**Bragg Peak**	**Tail**
^{11}C	350 MeV/u	15.1 ± 0.4	155 ± 2	38 ± 1
^{12}C	350 MeV/u	14.8 ± 0.3	192 ± 2	37 ± 2
^{15}O	250 MeV/u	24.7 ± 0.2	110 ± 0.7	-
^{16}O	430 MeV/u	21.1 ± 0.2	111 ± 0.3	-

Table 4: The experimentally-evaluated values of RBE_{10} in each region for the positron-emitting radioactive and stable isotopes of carbon and oxygen in a water phantom.

		$\mathbf{RBE}_{10}$		
Ion	**Energy**	**Entrance**	**Bragg Peak**	**Tail**
^{11}C	350 MeV/u	1.2 ± 0.1	2.7 ± 0.4	1.6 ± 0.2
^{12}C	350 MeV/u	1.2 ± 0.1	2.9 ± 0.4	1.5 ± 0.1
^{15}O	250 MeV/u	1.4 ± 0.1	2.7 ± 0.4	-
^{16}O	430 MeV/u	1.3 ± 0.1	2.8 ± 0.4	-

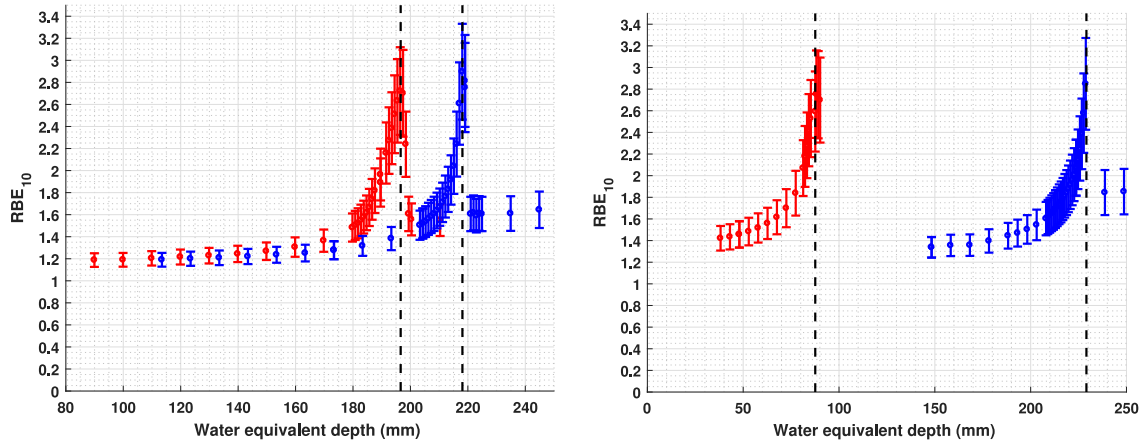

(a) Red = 350 MeV/u ^{11}C, blue = 350 MeV/u ^{12}C (b) Red = 250 MeV/u ^{15}O, blue = 430 MeV/u ^{16}O

Figure 4: RBE_{10} for the positron-emitting radioactive and stable isotopes of carbon and oxygen in a water phantom, plotted as a function of depth with 95% confidence intervals. The vertical dashed lines represent the positions of the Bragg peaks.

is approximately 17% higher in the entrance region than for ^{16}O (each mean value being outside the 95% confidence intervals of its counterpart), while being close to identical in the Bragg peak region (being lower by 0.81% for ^{15}O relative to ^{16}O, and just outside of each others' respective 95% confidence intervals). The discrepancy in the entrance region may be due to the lower energy of the ^{15}O ion beam (constrained by the limitations of the available beamline and radioactive ion production method), causing the microdosimetric spectrum measurements obtained in the entrance region to include some contribution from the build-up region. While y_D could not be evaluated in the tail region for the oxygen beams, this region receives the least dose of the three, and based on the other results obtained in this study and our previously published simulation-based estimates of the RBE_{10} of the radioactive beams[27], we do not expect significant deviations between the values of $\overline{y_D}$ for the stable and radioactive isotopes of oxygen in the tail region.

The RBE_{10} of ^{11}C and ^{12}C are in close agreement, with the mean value for each isotope being within the 95% confidence interval of the other in all three regions. Similarly, for ^{15}O and ^{16}O, the RBE_{10} values are within mutual 95% confidence intervals in the entrance and build-up/Bragg peak regions, with RBE_{10} not being evaluated for the tail reason (since we were unable to evaluate $\overline{y_D}$ in this region for oxygen).

The similarity in relative biological effectiveness calculated for the radioactive and stable heavy ion beams, particularly in the build-up/Bragg peak regions where the dose and dose gradients are highest, indicates that a radioactive positron-emitting ion species could be substituted for the corresponding stable isotope without significantly altering the biological effects. It is hypothesised that current treatment methods and treatment-planning systems could therefore be used to treat patients with radioactive heavy ion beams with minimal changes due to the near-equivalence of the RBE_{10}. These results closely agree with our previously reported theoretical/simulation results (2.7±0.4 experimental versus 2.9±0.5 simulated for ^{11}C, 2.9±0.4 vs. 3±0.2 for ^{12}C, 2.7± 0.4 vs. 2.4±0.2 for ^{15}O and 2.8±0.4 vs. 2.8±0.6 for ^{16})[27].

III.D. PET image quality

Total annihilation photon yield per incident primary particle measured by the in-beam whole-body DOI-PET imaging system are shown in Figure 5a for ^{11}C/^{12}C and Figure 5b for ^{15}O/^{16}O ion beams, respectively. Plots of dose deposited along the path of the beam (normalised to entrance dose) are overlaid on top. The correlation between the Bragg peak and the point at which the maximum density of annihilations is observed is much stronger for the radioactive beams, with the mean difference between the location of the Bragg peak (taken as the depth of maximum macroscopic dose) and the point at which the maximum density of annihilations is observed being 2.4±0.8 mm for ^{11}C and 0.9±0.8 mm for ^{15}O, compared to -5.6±0.8 mm for ^{12}C and -6.6±0.8 mm for ^{16}O. These results also demonstrate that the location of the point of maximum annihilation photon density is distal to the Bragg peak for the radioactive beams while proximal for the stable ion beams, which are in agreement with measurements previously reported by Mohammadi et al. and Augusto et al.[28,29]. This is a consequence of the PET signal from positron-emitting radioactive beams being dominated by unfragmented positron-emitting primary particles, which predominantly stop in the Bragg peak region. In contrast, positron annihilation yield resulting from stable ion irradiation is mainly due to fragmentation of the primary nuclei at the end of their path, resulting in lighter radioactive fragments which stop at a shorter range compared to the unfragmented heavier stable primary ion.

PET images acquired over 5 minutes and 20 minutes using each of the four beams are

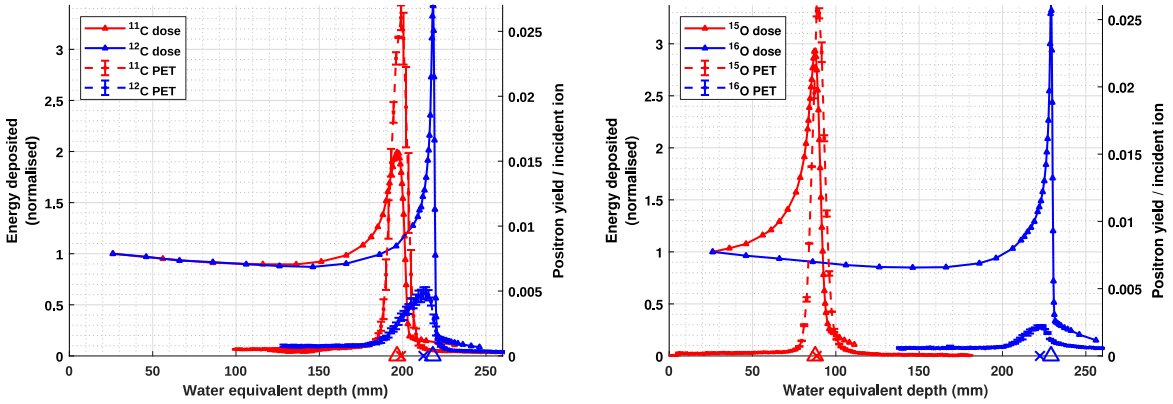

(a) Red = 350 MeV/u ^{11}C, blue = 350 MeV/u ^{12}C (b) Red = 250 MeV/u ^{15}O, blue = 430 MeV/u ^{16}O

Figure 5: Cumulative positron annihilations per incident primary particle and entrance-normalised dose as a function of depth for each ion beam. Depth of maximum dose is indicated with Δ; depth of maximum positron annihilation density is indicated with $\mathbf{x}$. Acquisition time was 20 minutes following final the spill.

shown in Figures 6 and 7, respectively. Image intensity is expressed in terms of positron yield per primary particle, with the same dynamic ranged used for all subfigures. The left-hand subfigures, corresponding to ^{11}C and ^{15}O, illustrate the precision with which the build-up/Bragg peak can be resolved when positron-emitting radioactive ion beams are used to deliver the dose. By contrast, the right-hand subfigures illustrate show that although the distal edge can be resolved quite accurately, the proximal edge is only weakly resolved, with poor contrast between the Bragg peak region and the entrance region (particularly for ^{12}C). This is because the entire yield of positron-emitting radionuclides in the field of view is due to non-elastic collisions along the entire path of the beam, whereas for the radioactive beams, the majority of positron yield is due to the decay of unfragmented primary particles at their stopping point (near the Bragg peak). The unfragmented primary particle component strongly dominates the signal in the Bragg peak region, while in the entrance region, positron yield is dominated by target fragmentation, which is similar for both stable and radioactive ion beams.

The signal-to-background ratio (SBR), defined as ratio between average intensity of subset of pixels with more than 90% of the peak yield per primary particle to the mean image intensity in the tail region, are shown for each ion species in Table 5. The tail region is considered as the background reference to illustrate the effectiveness of each beam type

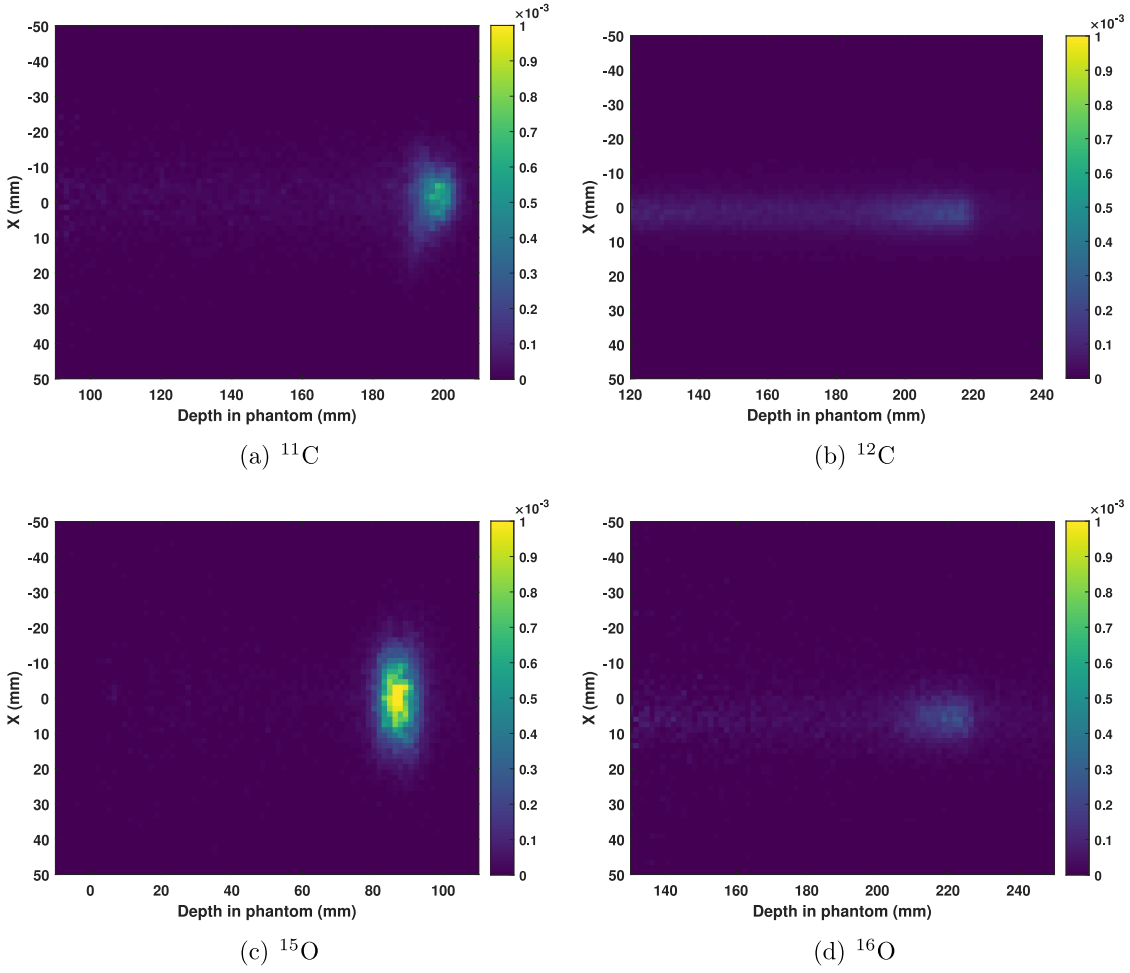

(a) ^{11}C (b) ^{12}C

(c) ^{15}O (d) ^{16}O

Figure 6: PET images for each beam type after 5 minutes of acquisition. Image intensity corresponds to the activity generated within the phantom per primary ion beam fluence (cumulative number of ions per cm^2).

Table 5: Peak-signal to background ratios

Isotope	**5 minutes**	**20 minutes**
^{11}C	4054	7390
^{12}C	404	670
^{15}O	20408	20474
^{16}O	3938	3970

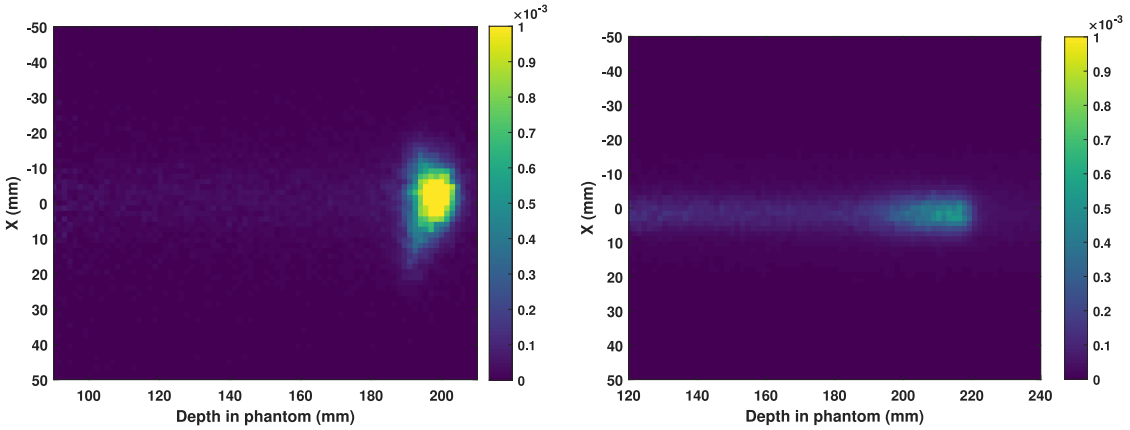

(a) ^{11}C (b) ^{12}C

(c) ^{15}O (d) ^{16}O

Figure 7: PET images for each beam type after 20 minutes of acquisition. Image intensity corresponds to the activity generated within the phantom per primary ion beam fluence (cumulative number of ions per cm^2).

for range verification; a similar enhancement in SBR is seen if the entrance region is used as the reference. The SBR for ^{11}C is better than that of ^{12}C by a factor of 10 and 11 after 5 and 20 minutes of image acquisition, respectively, while for ^{15}O is 5.18 and 5.15 times better than for ^{16}O for 5 and 20-minute acquisitions, respectively. These results are in very good agreement with our previously published simulation results[27].

IV. Conclusion

In this study, the microdosimetric dose-mean lineal energy $\overline{y_D}$ of therapeutic heavy ion beams of positron-emitting radioactive isotopes ^{11}C and ^{15}O (at 350 MeV/u and 250 MeV/u, respectively), and their corresponding stable ion species, ^{12}C and ^{16}O (at 350 MeV/u and 430 MeV/u), respectively was measured using the CMRP silicon-on-insulator mushroom microdosimeter in a water phantom, and hence the relative biological effectiveness was calculated for each beam. The RBE_{10} of the radioactive beams was found to be equivalent to those of their respective stable beams to within the 95% confidence interval in the entrance, peak and tail regions. The raw values of $\overline{y_D}$ of the radioactive ion beams were very similar to those of the stable beams in most cases, despite the different beam energies, energy spreads and beam sizes. Additionally, post-irradiation PET images for range verification were of much better quality when positron-emitting radioactive ion species are used instead of their stable counterparts, with 5 to 11-fold improvements observed in the signal-to-background ratio. The location of the annihilation peak also corresponds more closely with the location of the Bragg peak for the radioactive ions compared to stable ions. Therefore, with equivalent relative biological effectiveness and a large increase in statistics for quality assurance imaging, the use of positron emitting primary beams remains an enticing choice for use in heavy ion therapy.

Acknowledgements

This research has been conducted with the support of the Australian government research training program scholarship. The authors acknowledge the scientific assistance of the National Imaging Facility, a National Collaborative Research Infrastructure Strategy (NCRIS) capability, at the Australian Nuclear Science and Technology Organisation (ANSTO). The

authors would like to acknowledge the long term collaboration between the University of Wollongong's Centre for Medical Radiation physics and Norway's SINTEF research organisation, where the silicon-on-insulator mushroom microdosimeters were fabricated.

Conflict of Interest

The authors have no conflict of interest to disclose.

References

[1] O. Jäkel, D. Schulz-Ertner, C. Karger, A. Nikoghosyan, and J. Debus, Heavy Ion Therapy: Status and Perspectives, Technology in Cancer Research & Treatment **2**, 377–387 (2003).

[2] M. Durante and J. Loeffler, Charged particles in radiation oncology, Nat. Rev. Clin. Oncol. **7**, 37–43 (2009).

[3] M. Durante, R. Orecchia, and J. S. Loeffler, Charged-particle therapy in cancer: clinical uses and future perspectives, Nature Reviews Clinical Oncology **14**, 483–495 (2017).

[4] L. Sihver, D. Schardt, and T. Kanai, Depth-Dose Distributions of High-Energy Carbon, Oxygen and Neon Beams in Water, Jpn. J. Med. Phys. **18**, 1–21 (1998).

[5] M. Durante and H. Paganetti, Nuclear physics in particle therapy: a review, Reports on Progress in Physics **79**, 096702 (2016).

[6] Y. Kase, T. Kanai, Y. Matsumoto, Y. Furusawa, H. Okamoto, T. Asaba, M. Sakama, and H. Shinoda, Microdosimetric Measurements and Estimation of Human Cell Survival for Heavy-Ion Beams, Radiat. Res. **166**, 629–638 (2006).

[7] D. Schardt, T. Elsässer, and D. Schulz-Ertner, Heavy-ion tumor therapy: Physical and radiobiological benefits, Reviews of Modern Physics **82**, 383–425 (2010).

[8] M. Krämer and M. Scholz, Treatment planning for heavy-ion radiotherapy: calculation and optimization of biologically effective dose, Phys. Med. Biol. **45**, 3319–3330 (2000).

[9] Y. Iseki, H. Mizuno, Y. Futami, T. Tomitani, T. Kanai, M. Kanazawa, A. Kitagawa, T. Murakami, T. Nishio, M. Suda, E. Urakabe, A. Yunoki, and H. Sakai, Positron camera for range verification of heavy-ion radiotherapy, Nucl. Inst. Meth. A **515**, 840–849 (2003).

[10] Y. Iseki, T. Kanai, M. Kanazawa, A. Kitagawa, H. Mizuno, T. Tomitani, M. Suda, and E. Urakabe, Range verification system using positron emitting beams for heavy-ion radiotherapy, Phys. Med. Biol. **49**, 3179–3195 (2004).

[11] K. Parodi, H. Paganetti, H. A. Shih, S. Michaud, J. S. Loeffler, T. F. DeLaney, N. J. Liebsch, J. E. Munzenrider, A. J. Fischman, A. Knopf, and T. Bortfeld, Patient Study of In Vivo Verification of Beam Delivery and Range, Using Positron Emission Tomography and Computed Tomography Imaging After Proton Therapy, Int. J. Radiat. Oncol. Biol. Phys. **68**, 920–934 (2007).

[12] S. Combs, J. Bauer, D. Unholtz, C. Kurz, T. Welzel, D. Habermehl, T. Haberer, J. Debus, and K. Parodi, Monitoring of patients treated with particle therapy using positron-emission-tomography (PET): the MIRANDA study, BMC Cancer **12** (2012).

[13] J. Krimmer, D. Dauvergne, J. Létang, and É. Testa, Prompt-gamma monitoring in hadrontherapy: A review, Nuclear Instruments and Methods in Physics Research Section A: Accelerators, Spectrometers, Detectors and Associated Equipment **878**, 58–73 (2018).

[14] T. Hofmann, M. Pinto, A. Mohammadi, M. Nitta, F. Nishikido, Y. Iwao, H. Tashima, E. Yoshida, A. Chacon, M. Safavi-Naeini, A. Rosenfeld, T. Yamaya, and K. Parodi, Dose reconstruction from PET images in carbon ion therapy: a deconvolution approach, Phys. Med. Biol. **64**, 025011 (2019).

[15] H. D. Maccabee, U. Madhvanath, and M. R. Raju, Tissue activation studies with alpha-particle beams, Phys. Med. Biol. **14**, 213–224 (1969).

[16] A. Kraan, G. Battistoni, N. Belcari, N. Camarlinghi, G. Cirrone, G. Cuttone, S. Ferretti, A. Ferrari, G. Pirrone, F. Romano, P. Sala, G. Sportelli, K. Straub, A. Tramontana, A. D. Guerra, and V. Rosso, Proton range monitoring with in-beam PET: Monte Carlo activity predictions and comparison with cyclotron data, Physica Medica **30**, 559–569 (2014).

[17] A. Chacon, S. Guatelli, H. Rutherford, D. Bolst, A. Mohammadi, A. Ahmed, M. Nitta, F. Nishikido, Y. Iwao, H. Tashima, E. Yoshida, G. Akamatsu, S. Takyu, A. Kitagawa, T. Hofmann, M. Pinto, D. R. Franklin, K. Parodi, T. Yamaya, A. Rosenfeld, and M. Safavi-Naeini, Comparative study of alternative Geant4 hadronic ion inelastic physics models for prediction of positron-emitting radionuclide production in carbon and oxygen ion therapy, Phys. Med. Biol. **64**, 155014 (2019).

[18] G. Kraft, U. Arndt, W. Becher, D. Schardt, H. Stelzer, U. Weber, and T. Archinal, Heavy ion therapy at GSI, Nucl. Inst. Meth. A **367**, 66–70 (1995).

[19] E. Yoshida, H. Tashima, T. Shinaji, K. Shimizu, H. Wakizaka, A. Mohammadi, F. Nishikido, and T. Yamaya, Development of a Whole-Body Dual Ring OpenPET for in-Beam PET, IEEE T Radiat Plasma Med Sci **1**, 293–300 (2017).

[20] E. Urakabe, T. Kanai, M. Kanazawa, A. Kitagawa, K. Noda, T. Tomitani, M. Suda, Y. Iseki, K. Hanawa, K. Sato, M. Shimbo, H. Mizuno, Y. Hirata, Y. Futami, Y. Iwashita, and A. Noda, Spot Scanning Using Radioactive ^{11}C Beams for Heavy-Ion Radiotherapy, Jpn. J. Appl. Phys. **40**, 2540–2548 (2001).

[21] M. Kanazawa, A. Kitagawa, S. Kouda, T. Nishio, M. Torikoshi, K. Noda, T. Murakami, M. Suda, T. Tomitani, T. Kanai, Y. Futami, M. Shinbo, E. Urakabe, and Y. Iseki, Application of an RI-beam for cancer therapy: In-vivo verification of the ion-beam range by means of positron imaging, Nucl. Phys. A **701**, 244–252 (2002).

[22] S. Hojo, T. Honma, Y. Sakamoto, and S. Yamada, Production of ^{11}C-beam for particle therapy, Nucl. Inst. Meth. B **240**, 75–78 (2005).

[23] M. Lazzeroni and A. Brahme, Production of pure quasi-monochromatic ^{11}C beams for accurate radiation therapy and dose delivery verification, Nucl. Inst. Meth. B **359**, 120–130 (2015).

[24] R. Augusto, T. Mendonca, F. Wenander, L. Penescu, R. Orecchia, K. Parodi, A. Ferrari, and T. Stora, New developments of 11 C post-accelerated beams for hadron therapy and imaging, Nucl. Inst. Meth. B **376**, 374–378 (2016).

[25] K. Katagiri, A. Noda, K. Nagatsu, M. Nakao, S. Hojo, M. Muramatsu, K. Suzuki, T. Wakui, and K. Noda, A singly charged ion source for radioactive ^{11}C ion acceleration, Rev. Sci. Instrum. **87**, 02B509 (2016).

[26] A. Mohammadi, E. Yoshida, H. Tashima, F. Nishikido, T. Inaniwa, A. Kitagawa, and T. Yamaya, Production of an ^{15}O beam using a stable oxygen ion beam for in-beam PET imaging, Nucl. Inst. Meth. A **849**, 76–82 (2017).

[27] A. Chacon, M. Safavi-Naeini, D. Bolst, S. Guatelli, D. R. Franklin, Y. Iwao, G. Akamatsu, H. Tashima, E. Yoshida, F. Nishikido, A. Kitagawa, A. Mohammadi, M.-C. Gregoire, T. Yamaya, and A. B. Rosenfeld, Monte Carlo investigation of the characteristics of radioactive beams for heavy ion therapy, Sci. Rep. **9**, 6537–6549 (2019).

[28] R. S. Augusto, A. Mohammadi, H. Tashima, E. Yoshida, T. Yamaya, A. Ferrari, and K. Parodi, Experimental validation of the FLUKA Monte Carlo code for dose and β^+-emitter predictions of radioactive ion beams, Phys. Med. Biol. **63**, 215014 (2018).

[29] A. Mohammadi, H. Tashima, Y. Iwao, S. Takyu, G. Akamatsu, F. Nishikido, E. Yoshida, A. Kitagawa, K. Parodi, and T. Yamaya, Range verification of radioactive ion beams of ^{11}C and ^{15}O using in-beam PET imaging, Phys. Med. Biol. **64**, 145014 (2019).

[30] Y. Kase, W. Yamashita, N. Matsufuji, K. Takada, T. Sakae, Y. Furusawa, H. Yamashita, and S. Murayama, Microdosimetric calculation of relative biological effectiveness for design of therapeutic proton beams, Radiat. Res. **54**, 485–493 (2012).

[31] A. B. Rosenfeld, Novel detectors for silicon based microdosimetry, their concepts and applications, Nucl. Inst. Meth. A **809**, 156–170 (2016).

[32] L. T. Tran, D. Bolst, S. Guatelli, A. Pogossov, M. Petasecca, M. L. F. Lerch, L. Chartier, D. A. Prokopovich, M. I. Reinhard, M. Povoli, A. Kok, V. L. Perevertaylo, N. Matsufuji, T. Kanai, M. Jackson, and A. B. Rosenfeld, The relative biological effectiveness for carbon, nitrogen, and oxygen ion beams using passive and scanning techniques evaluated with fully 3D silicon microdosimeters, Med. Phys. **45**, 2299–2308 (2018).

[33] L. T. Tran, L. Chartier, D. Bolst, J. Davis, D. A. Prokopovich, A. Pogossov, S. Guatelli, M. I. Reinhard, M. Petasecca, M. L. Lerch, N. Matsufuji, M. Povoli, A. Summanwar,

A. Kok, M. Jackson, and A. B. Rosenfeld, In-field and out-of-file application in ^{12}C ion therapy using fully 3D silicon microdosimeters, Radiat. Meas. **115**, 55–59 (2018).

[34] G. Akamatsu, H. Tashima, Y. Iwao, H. Wakizaka, T. Maeda, A. Mohammadi, S. Takyu, M. Nitta, F. Nishikido, H. Rutherford, A. Chacon, M. Safavi-Naeini, E. Yoshida, and T. Yamaya, Performance evaluation of a whole-body prototype PET scanner with four-layer DOI detectors, Phys. Med. Biol. **64**, 095014 (2019).

[35] D. Bolst, S. Guatelli, L. T. Tran, L. Chartier, M. L. F. Lerch, N. Matsufuji, and A. B. Rosenfeld, Correction factors to convert microdosimetry measurements in silicon to tissue in ^{12}C ion therapy, Phys. Med. Biol. **62**, 2055–2069 (2017).

[36] K. U. Kobayashi, N. Oikawa, and R. Kurita, Dynamical transition of heat transport in a physical gel near the sol-gel transition, Sci. Rep. **5** (2015).

[37] J. Bauer, D. Unholtz, C. Kurz, and K. Parodi, An experimental approach to improve the Monte Carlo modelling of offline PET/CT-imaging of positron emitters induced by scanned proton beams, Phys. Med. Biol. **58**, 5193–5213 (2013).